Appl. Phys. B (2017) 123:221
DOI 10.1007/s00340-017-6790-z

Applied Physics B
Lasers and Optics

Mechanically deposited tungsten disulfide saturable absorber for low-threshold Q-switched erbium-doped fiber laser

K. Y. Lau[1] · A. A. Latif[2] · M. H. Abu Bakar[1] · F. D. Muhammad[2] · M. F. Omar[3] · M. A. Mahdi[1]

Received: 9 November 2016 / Accepted: 11 July 2017 / Published online: 27 July 2017

Abstract In this paper, we report a Q-switched erbium-doped fiber laser incorporating tungsten disulfide (WS_2) as the saturable absorber. A direct mechanical deposition technique using a scotch tape is employed to place the WS_2 powder onto the tip of a fiber ferrule. Several runs of mechanical extraction are performed to reduce the thickness of WS_2 powder on the fiber tip. The fabricated WS_2 saturable absorber exhibits a saturation intensity of 548.6 MW/cm^2, modulation depth of 4.1% and non-saturable loss of 67.8%. A ring cavity erbium-doped fiber laser integrating the WS_2 saturable absorber yields continuous wave lasing and Q-switching threshold at pump power of 10 and 12.7 mW, respectively. This Q-switching pump power threshold is the lowest to the best of the authors' knowledge. The proposed technique of direct mechanical deposition is inexpensive, significantly faster and simpler compared to previously reported methods.

1 Introduction

Passively Q-switched fiber laser is of great interest among researchers due to its contribution in material processing, biomedical diagnoses, distance measurement, three-dimensional optical data storage, tattoo removal, and laser cutting [1–4]. Such applications capitalize on Q-switch typical characteristics of pulse width and pulse energy in microsecond and nanojoule ranges, respectively [5].

Passively Q-switched fiber laser is generated by employing a saturable absorber (SA). Presently, layered structured materials or two-dimensional (2D) materials have attracted substantial research interest as SA [6]. This includes graphene [7–9], topological insulators (TIs) [10–12], and transition metal dichalcogenides (TMDs) [13], which are highly coveted due to their high third-order nonlinear susceptibility and ultrafast carrier dynamics [14–17]. Graphene possesses zero bandgap and linear dispersion of Dirac electrons essential for broadband saturable absorption [18]. However, graphene suffers from intrinsic shortcoming due to its gapless behavior which imposes limitation in optoelectronics application. On the other hand, TI has been discovered to exhibit electronic bandgap and gapless Dirac edge states confined by its topological symmetry [6]. TI is an unusual quantum state of matter, determined by the formation of its surface or at edges where time-reversal symmetry shields the TI gapless metallic state [19]. These states are structured by the topological effects in which the impurities scattering are minimized when electrons travel on such surfaces [12]. Nevertheless, preservation of the unique surface states of TI has been a concern during dominant bulk conduction and its susceptibility to contamination in ambient atmosphere increases operational complexity and limitation for multiple device applications [20]. Recently, black phosphorus (BP) was demonstrated with narrow spectral bandwidth and Q-switched instability peaks at central wavelength of 1562.9 nm [21]. Based on the report in [17], BP has significant drawback in terms of poor material stability, making it less attractive for certain applications.

✉ M. A. Mahdi
mam@upm.edu.my

[1] Wireless and Photonics Network Research Center, Faculty of Engineering, Universiti Putra Malaysia, 43400 UPM Serdang, Selangor, Malaysia

[2] Department of Physics, Faculty of Science, Universiti Putra Malaysia, 43400 UPM Serdang, Selangor, Malaysia

[3] Physics Department, Faculty of Science, Universiti Teknologi Malaysia, 81310 Skudai, Johor, Malaysia

As a result, current research has been primarily focused on the TMD, owing to their diversity and layer-dependent characteristics, which is analogous or even superior to the zero bandgap property of graphene [14, 22]. Examples of TMD include molybdenum disulfide (MoS_2), molybdenum diselenide ($MoSe_2$), tungsten disulfide (WS_2), and tungsten diselenide (WSe_2). These materials are indirect semiconductor in bulky states, which are structured by hexagonal metal atoms layered between two layers of chalcogens [23]. The inter-plane layers of the prismatic trigonal TMD are held by weak van der Waals' force, which lubricates the TMD layers allowing them to slide off easily and make them possible to be exfoliated into single and few layer forms. Since the bandgap of TMDs is largely determined by the layer thickness, the optical properties of TMDs can thus be engineered to meet the desired performances. Monolayer TMDs possess gapless or direct electronic bandgap and thus can still provide complementary properties to graphene, such as wide saturable absorption, in addition to their robustness and environmental stability. Recently, TMD has been successfully utilized to generate passively Q-switched [24, 25] and mode-locked lasers [26–28] thanks to its remarkable optical and optoelectronics

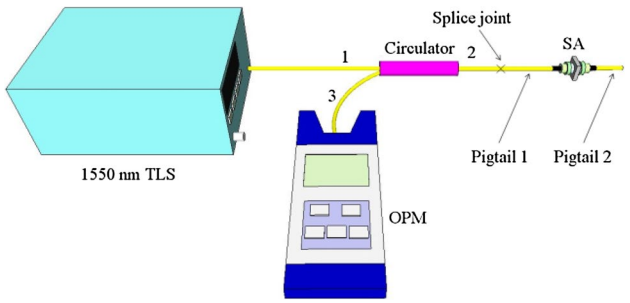

Fig. 1 Schematic diagram of the in situ power monitoring for optical extraction forming desirable WS_2 layer on the fiber ferrule end

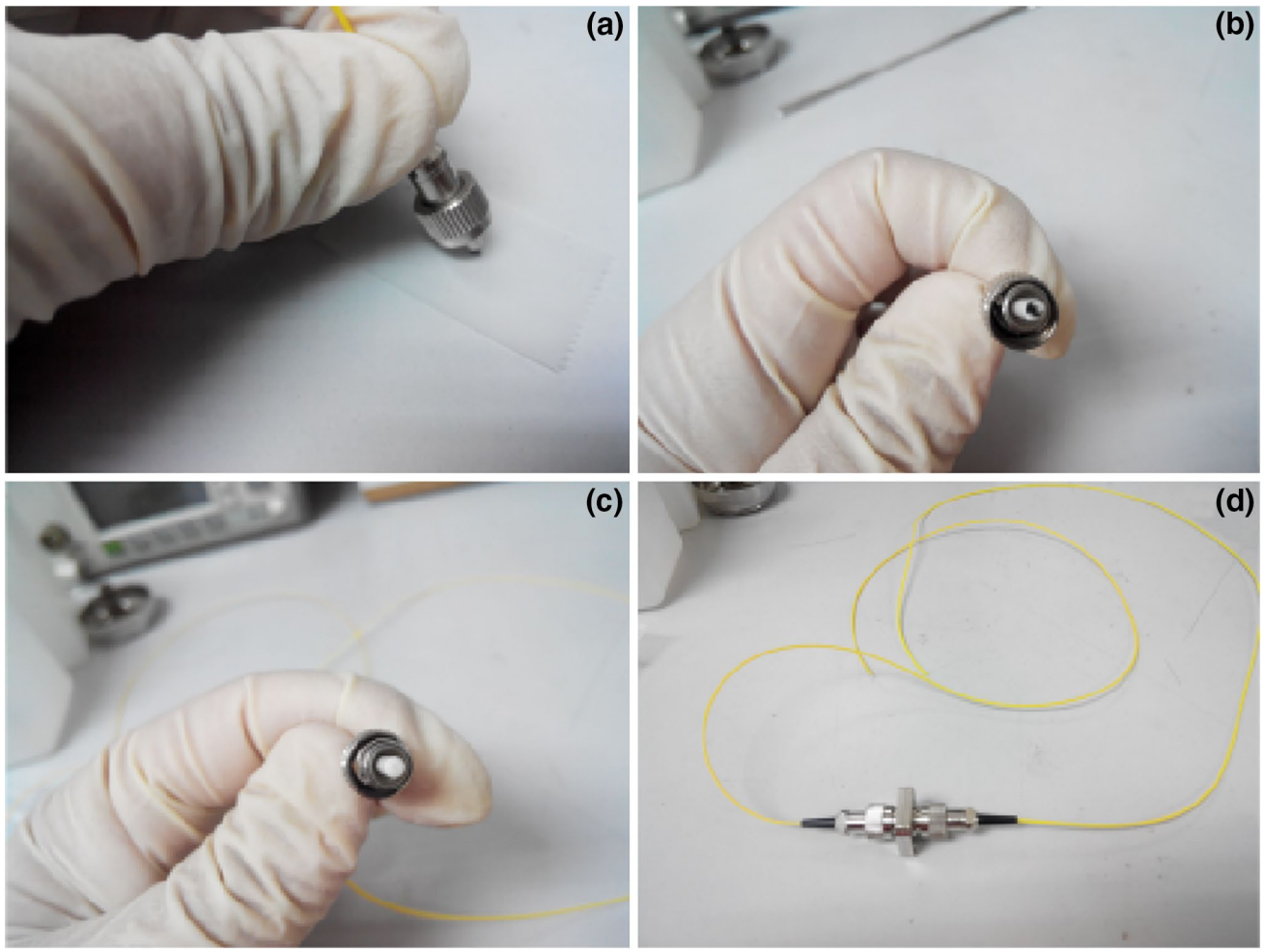

Fig. 2 **a** WS_2 nano-powder on the scotch tape attached to SMF-28 fiber ferrule, **b** thick layers of WS_2 observed on the fiber ferrule, **c** post-exfoliation of WS_2 layers and **d** the formation of WS_2-SA by connecting two SMF-28 pigtails

properties, specifically on the nonlinear light absorption ability. In addition, the thermal conductivity of WS_2 is 2.2 Wm^{-1} K^{-1} (*bulk material*), which is thermally stable at high pump power. Considering the similarity of WS_2 and MoS_2, the latter TMD material possesses lower thermal conductivity of 1.05 Wm^{-1} K^{-1} (*bulk material*), which is less stable at high pump power resulting in the presence of instability peaks in MoS_2-SA-based Q-switched laser [29]. Therefore, WS_2-SA is selected in our proposal as a Q-switcher to overcome the thermal stability issue using MoS_2-SA.

Although there have been numerous reports on WS_2-SA in pulsed fiber laser, prior integrations of WS_2-SA into the fiber laser system require sophisticated approaches such as incorporating WS_2-polyvinyl alcohol (PVA) thin film on a sandwiched structure between two fiber pigtails [24], evanescent field interaction with microfiber [25], and by injecting WS_2 suspension into air channels around the solid core of a photonic crystal fiber (PCF) [28]. These approaches require skillful operation and highly precise instrumentation, thereby making the fabrication process difficult. Here, we propose a new technique to deposit the WS_2 nano-sized monolayer powder mechanically onto the fiber ferrule. To the best of our knowledge, this is the first demonstration of direct mechanical deposition technique by attaching WS_2 nano-powder onto fiber ferrule as SA for Q-switched erbium-doped fiber laser (EDFL). This method is inexpensive, simple, and highly convenient as it allows the WS_2-SA to be immediately used after the fabrication process.

2 Fabrication and characterization of WS_2-SA

The nano size monolayer WS_2 powder from ACS Material, LLC is prepared by lithium-based intercalation method. The small size WS_2 powder appears black in nature with a diameter of 20–500 nm, thickness of approximately 1 nm, and monolayer ratio of more than 95%. To fabricate the SA, a small amount of WS_2 nano-powder is taken using a spatula and placed on a scotch tape. The fiber ferrule of a single

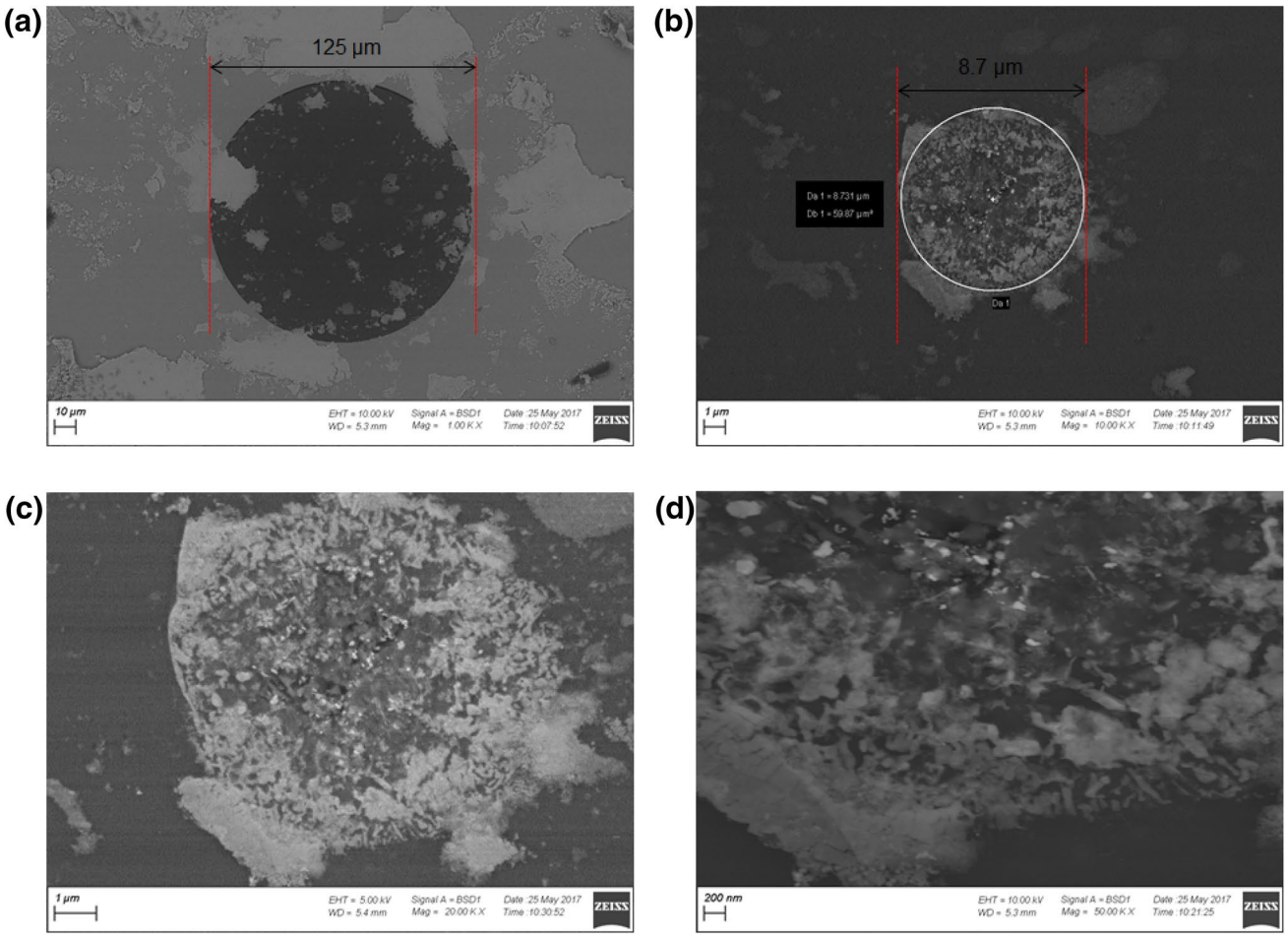

Fig. 3 FESEM images with magnification sizes of **a** ×1000, **b** ×10,000, **c** ×20,000, and **d** ×50,000

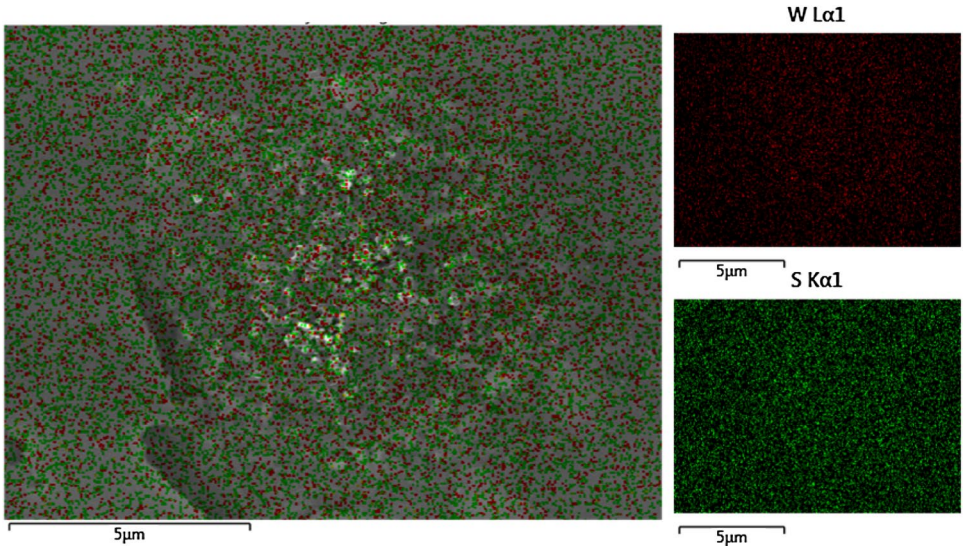

Fig. 4 EDX image of material distribution on the FIB-SEM image with magnification size of ×20,000

mode fiber (SMF-28 type) FC/PC pigtail is then dipped in the WS_2 nano-powder on the scotch tape. At this point, stacks of the monolayer WS_2 nano-powder are attached to the core area of fiber ferrule [30]. The thickness of the deposited monolayer WS_2 is then reduced through repeated exfoliation using clean scotch tape. Each run of this process is monitored in real time using reflection power from the pigtail, which correlates to the thickness of the monolayer WS_2 deposited onto the fiber ferrule. The schematic diagram for this in situ power monitoring is shown in Fig. 1. A 1550 nm laser source with power of 8 dBm is launched into an optical circulator and the reflected light from the pigtail is monitored through an optical power meter (OPM). This process is conducted until the reflected power is about 8%, half of which is contributed to Fresnel reflection, while the remaining 4% is due to the deposited WS_2. Once the desirable thickness of WS_2 is obtained, the WS_2-deposited pigtail is joined together with another SMF-28 pigtail through a fiber adaptor. Figure 2a–d illustrates the process of WS_2 SA fabrication by direct mechanical deposition method.

2.1 Morphology analysis

The WS_2-imprinted fiber ferrule morphology is observed using Zeiss Crossbeam 340 field emission scanning electron microscope (FESEM) system and the images are as illustrated in Fig. 3. All images are obtained using backscattering electron (BSE) detector to get good element contrast. WS_2 compounds have heavier atomic number compared to optical fiber material (SiO_2); thus, WS_2 will appear brighter with respect to the optical fiber in the BSE imaging mode. Figure 3a depicts the BSE image taken with a magnification size of ×1000. The circle with diameter measurement of 125 μm annotates the boundary of the fiber cladding region. WS_2 fragments are observed due to the force applied to the imprinted WS_2 powder during the exfoliation process. A closer look at the fiber core region with 8.7 μm diameter is achieved through a magnification size of ×10,000 as portrayed in Fig. 3b. A cluster of materials is observed at the fiber core region. These material clusters are uneven in thickness and the material flakes are observed with magnification sizes of ×20,000 and ×50,000 as shown in Fig. 3c, d, respectively.

2.2 Elemental analysis

Elemental characterization of the nanosheets is performed by energy-dispersive X-ray (EDX) mapping using Oxford Instruments X-Max^N. During the characterization, 20 kV acceleration voltage is used to excite the sample.

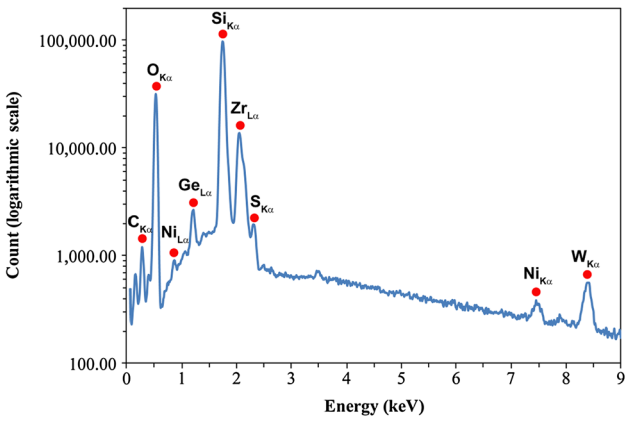

Fig. 5 EDX spectrum of material composition of the deposited WS_2 on the fiber ferrule

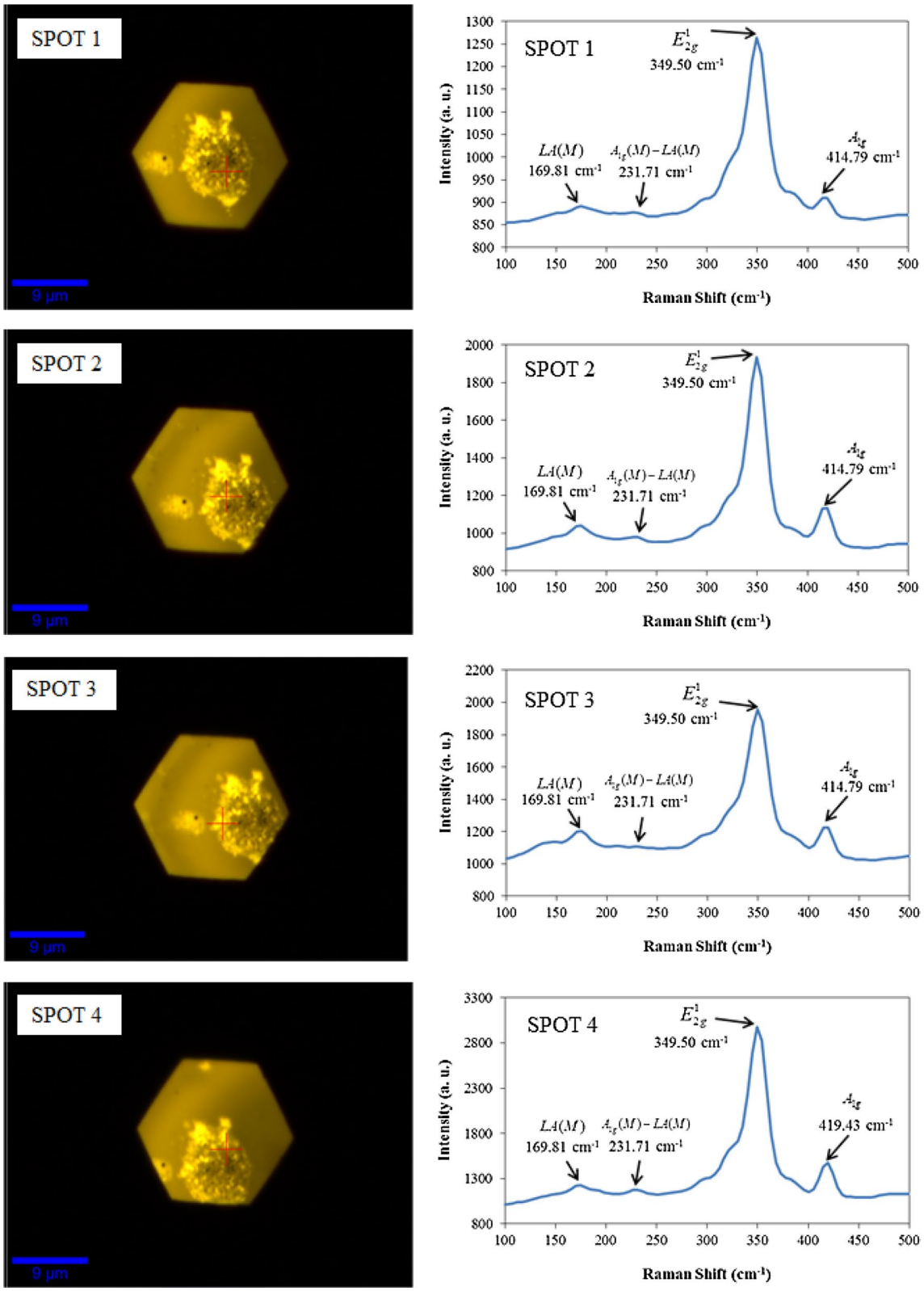

Fig. 6 Raman spectra of randomly selected spots of WS_2 nano-powder deposited on the fiber core

Figure 4 shows the overlay of EDX elemental mapping for tungsten (W, red color) and sulfur (S, green color) with BSE image at ×20,000 magnification size (Fig. 3c). The WS_2 composition is determined using characteristic x-ray $W_{L\alpha}$ (8.40 keV) and $S_{K\alpha}$ (2.31 keV). The distribution profile of W and S observed in Fig. 4 validates the feasibility of the proposed fabrication procedure.

The EDX spectrum of material composition from Fig. 4 is delineated in Fig. 5. Based on this spectrum, the highest counts are observed with elements silicon (Si) and oxygen (O), which are the base materials for the silica optical fiber. Germanium (Ge) detected in the scanned region is a common dopant in optical fibers. The element zirconia (Zr) is associated with the ceramic zirconia fiber ferrule used in the experiment. A small amount of nickel (Ni) is detected due to the presence of stage holder during the measurement. From Fig. 5, the peaks of S and W are observed at the K-series line and L-series line, respectively. By neglecting other elements, the atomic percentage of S is 60.76% and 39.24% is attributed to W. Unfortunately, these values do not lead directly to WS_2. This may be due to the internal absorption of $S_{K\alpha}$ X-ray. Since *W* is a heavy element which has high absorption coefficient, some low-energy $S_{K\alpha}$ X-ray is absorbed by nearby W atom before escaping the film's surface. This leads to lower $S_{K\alpha}$ X-ray intensity arriving at the EDX detector. Taking into account this phenomenon, the element composition can be approximated to WS_2, which is our main deposited element.

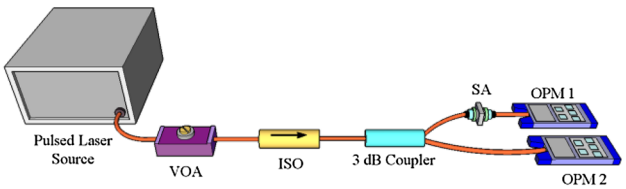

Fig. 7 Experimental setup to characterize nonlinear saturable absorption of WS_2-SA

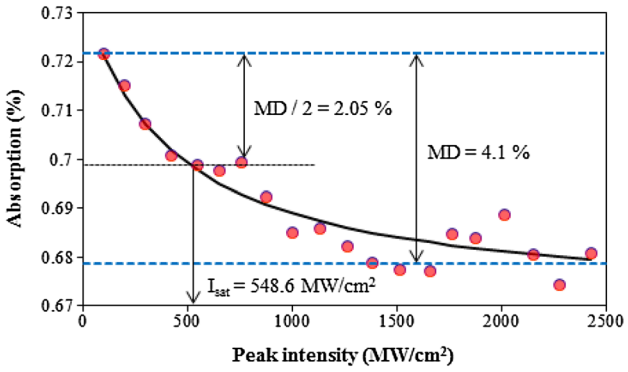

Fig. 8 Nonlinear saturable absorption characteristics of WS_2-SA. (*MD* modulation depth, I_{sat} saturation intensity)

2.3 Raman spectroscopy

The number of WS_2 layers of four selected spots on the fiber core is determined from the Raman spectrum as illustrated in Fig. 6. This Raman spectrum is generated using an Alpha 300R Raman Spectroscopy with excitation wavelength of 532.17 nm. The spectrum is dominated by the second-order modes with LA(M) at approximately 169.81 cm^{-1}, A_{1g}(M)-LA(M) at 231.71 cm^{-1}, E^1_{2g} mode at 349.50 cm^{-1}, and A_{1g} mode at 414.79 cm^{-1}. The LA indicates the longitudinal acoustic mode and the symbol (M)

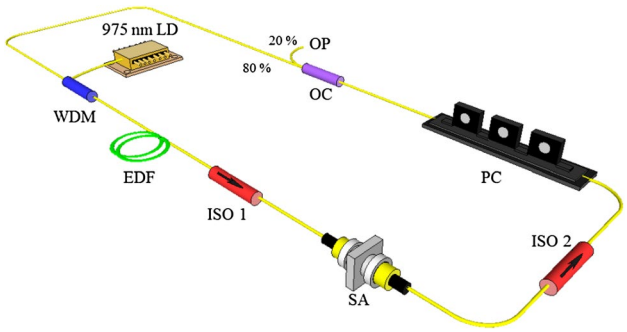

Fig. 9 Ring configuration of Q-switched pulse EDFL using WS_2-SA

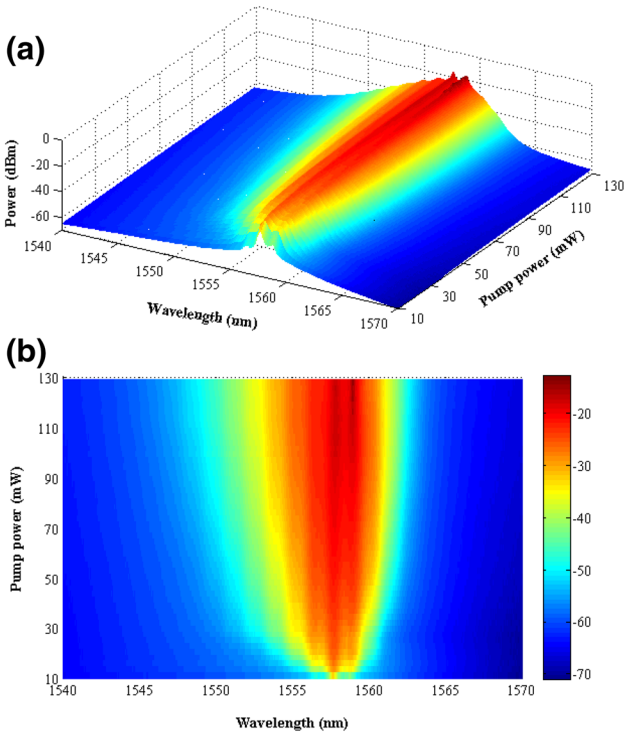

Fig. 10 **a** Optical spectrum of the WS_2-SA-based Q-switched EDFL as a function of pump power and **b** *top view* of Q-switched EDFL optical spectrum

describes the specific direction and magnitude of the phonon momentum [31]. Based on Ref. [32], monolayer WS_2 is confirmed at three chosen spots (SPOT 1-3) with the frequency difference between E^1_{2g} and A_{1g} of approximately 65.29 cm^{-1}. However, the frequency difference between E^1_{2g} and A_{1g} for SPOT 4 is 69.93 cm^{-1}. This value is close to the bulk material value of 70 cm^{-1} as reported in Ref. [32]. Therefore, this result indicates that there are multiple layers of WS_2 at SPOT 4. It can be concluded from the Raman spectroscopic results that the fiber core surface consists of WS_2 layers with uneven thickness.

2.4 Nonlinear saturable absorption

The experimental setup to measure the nonlinear saturable absorption of the WS_2-SA is depicted in Fig. 7. In this experiment, a 1550 nm pulsed laser source is employed with pulse duration and pulse repetition rate of 600 fs and 11.3 MHz, respectively. A variable optical attenuator (VOA) is used to adjust the power of the pulsed laser source. An isolator is fusion spliced from the output port of the VOA to a 50/50 coupler to prevent any reflected signal from returning to the pulsed laser source. The 50/50 coupler is utilized to split the pulse signal into two paths. The first optical path is connected to the fabricated WS_2-SA, which is then connected to an optical power meter (OPM 1) and the other optical path is connected directly to another optical power meter (OPM 2). The optical detection at OPM 2 is labeled as the reference power and the reading from OPM 1 is referred to as the saturable absorption characteristics of the SA.

The nonlinear saturable absorption characteristic curve is illustrated in Fig. 8. Based on this figure, the modulation

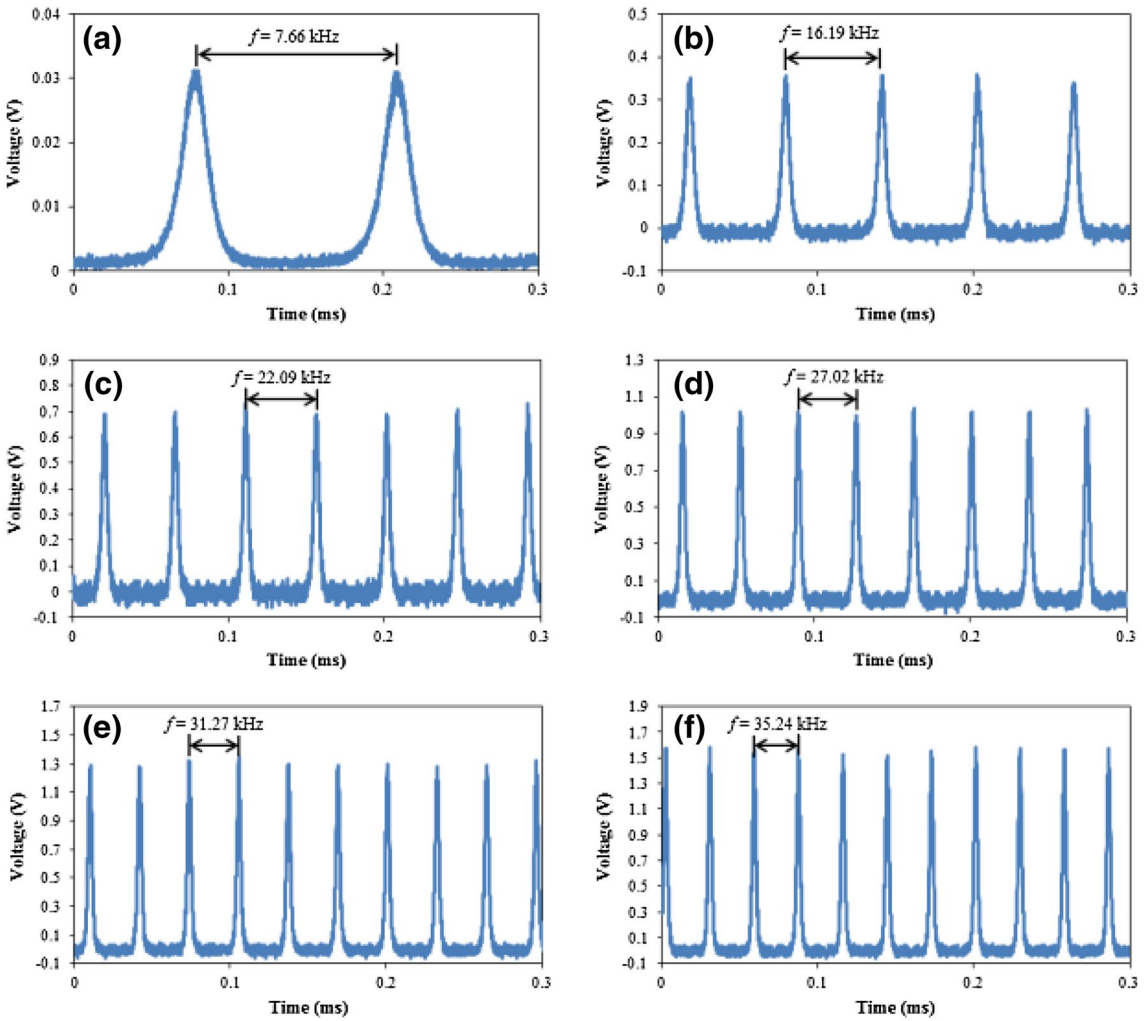

Fig. 11 Oscilloscope trace of Q-switched EDFL incorporating WS_2-SA at the pump power of **a** 12.7 mW, **b** 35.9 mW, **c** 58.8 mW, **d** 81.6 mW, **e** 104.7 mW, and **f** 128.8 mW

depth of the WS_2-SA is calculated at 4.1%, which is higher than the previously reported values of 0.3–0.5% [26], 1.2% [27], 2.53% [29], 2.96% [24], and 3.53% [28]. In addition, the saturation intensity and non-saturable loss achieved by the WS_2-SA is 548.6 MW/cm^2 and 67.8%, respectively.

3 Fiber laser setup

Figure 9 illustrates the EDFL experimental setup with ring configuration, which is used to verify the functionality of the fabricated WS_2-SA. The total cavity length employed for the EDFL cavity is 18.3 m, which consists of 5 m-long Lucent HP-980 erbium-doped fiber (EDF), 1 m-long Hi-1060 fiber, and 12.3 m-long SMF-28 fiber. A 975 nm laser diode (LD) provides the excitation to the EDF and is coupled through a 980/1550 nm wavelength division multiplexer (WDM). The common port of WDM is fusion spliced to the Hi-1060 fiber which is then connected to the EDF. The EDF has signal absorption coefficient of 3.5 dB/m at 1530 nm and −18 ps/nm/km dispersion coefficients. In the setup, all joints are fusion spliced except for the SA. Since the SA is formed by joining two fiber ferrules, this device is exposed to Fresnel reflections, which can disrupt the laser stability. To minimize this effect, the SA is placed in between two isolators (ISO 1 and ISO 2). These isolators have the same orientation to maintain unidirectional signal oscillation (clockwise direction) in the cavity. Polarization controller (PC) is inserted after ISO 2 to reduce the cavity birefringence effect by adjusting the signal polarization state. To complete the ring loop, a fiber coupler (OC) is placed in between the PC and the WDM. For this setup, 80% of the signal power is coupled back to the ring cavity and the remaining 20% signal power (OP) is extracted out for further analysis.

4 Fiber laser performance

Figure 10a depicts the optical spectrum of WS_2-SA-based Q-switched EDFL as a function of pump power. In addition, the top view of this Q-switched EDFL optical spectrum is illustrated in Fig. 10b. The continuous wave laser is initiated at threshold pump power of 10 mW. By adding more pump power, the cavity starts operating in the Q-switched laser regime at pump power threshold of 12.7 mW. The Q-switching threshold of WS_2-SA in this research work is significantly lower than those achieved by few-layers WS_2 nanosheets-coated side-polished fiber [25] and WS_2-PVA thin film sandwiched between fiber ferrules [29], which achieved Q-switching threshold values of 207.4 and 400 mW, respectively. Wider spectral bandwidth is observed with higher pump power and the Q-switched laser is well maintained at the maximum pump power of 128.8 mW. In particular, the spectral bandwidth evolves from 0.5 nm at 12.7 mW pump power to 2.6 nm at 128.8 mW pump power. However, two strong peaks emerge around 1558–1559 nm, indicating the presence of continuous wave (CW) laser signal. Despite the existence of CW components, stable pulse operation can still be obtained.

To verify the pulsing operation, measured oscilloscope trace of the Q-switched laser output is illustrated in Fig. 11. At lower pump power, the pulse width appears wider and vice versa. Contrary to mode-locked laser operation with constant pulse repetition rate, the pulse repetition rate of Q-switched EDFL depends on the pumped gain medium [33]. Consequently, higher pump power leads to faster round-trip time of the oscillated pulse [34].

A further analysis on the pulse repetition rate and pulse width of the WS_2-SA-based Q-switched EDFL

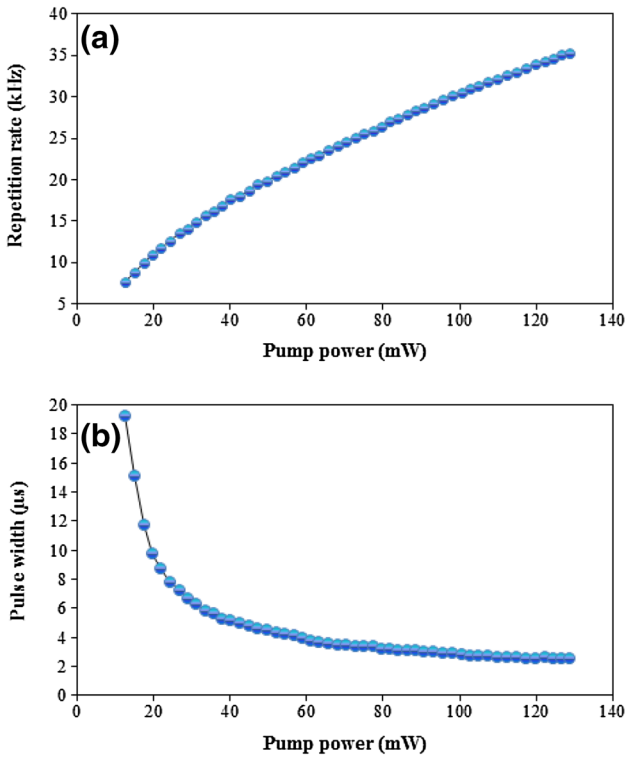

Fig. 12 **a** Pulse repetition rate and **b** pulse width of WS_2-SA-based Q-switched EDFL as a function of pump power

against the pump powers is depicted in Fig. 12. Based on Fig. 12a, the pulse repetition rate in an almost linear trend line as a function of pump power, from 7.7 kHz at pump power of 12.7 mW to 35.2 kHz at the maximum pump power of 128.8 mW. Since the saturation level governs pulse generation, increasing the pump power manifests higher repetition rate [35]. Additionally, the pulse width narrows down from 19.3 µs at 12.7 mW pump power to 2.6 µs at 128.8 mW pump power. The decreased pulse width as a function of pump power can be explained by strong pump-induced gain compression effect [36]. It is expected that by optimizing the cavity length, the pulse width can be further reduced.

The radio frequency (RF) spectrum of the WS_2-SA-based Q-switched EDFL is portrayed in Fig. 13. The RF measurement is taken with a resolution bandwidth of 10 Hz. The peak-to-pedestal extinction ratio (PER) is the contrast ratio measured from the peak level of the desired signal to the highest level of background noise. Based on Fig. 13, the PER increases in tandem with the increment of pump power. Therefore, the Q-switched EDFL possesses higher laser stability at higher pump power. In addition, the pulse width decreases as a function of pump power which validates the experimental results depicted in Fig. 11. At 128.8 mW pump power, 43.1 dB PER is obtained, which is comparable to previous PER values ranging from 40 to

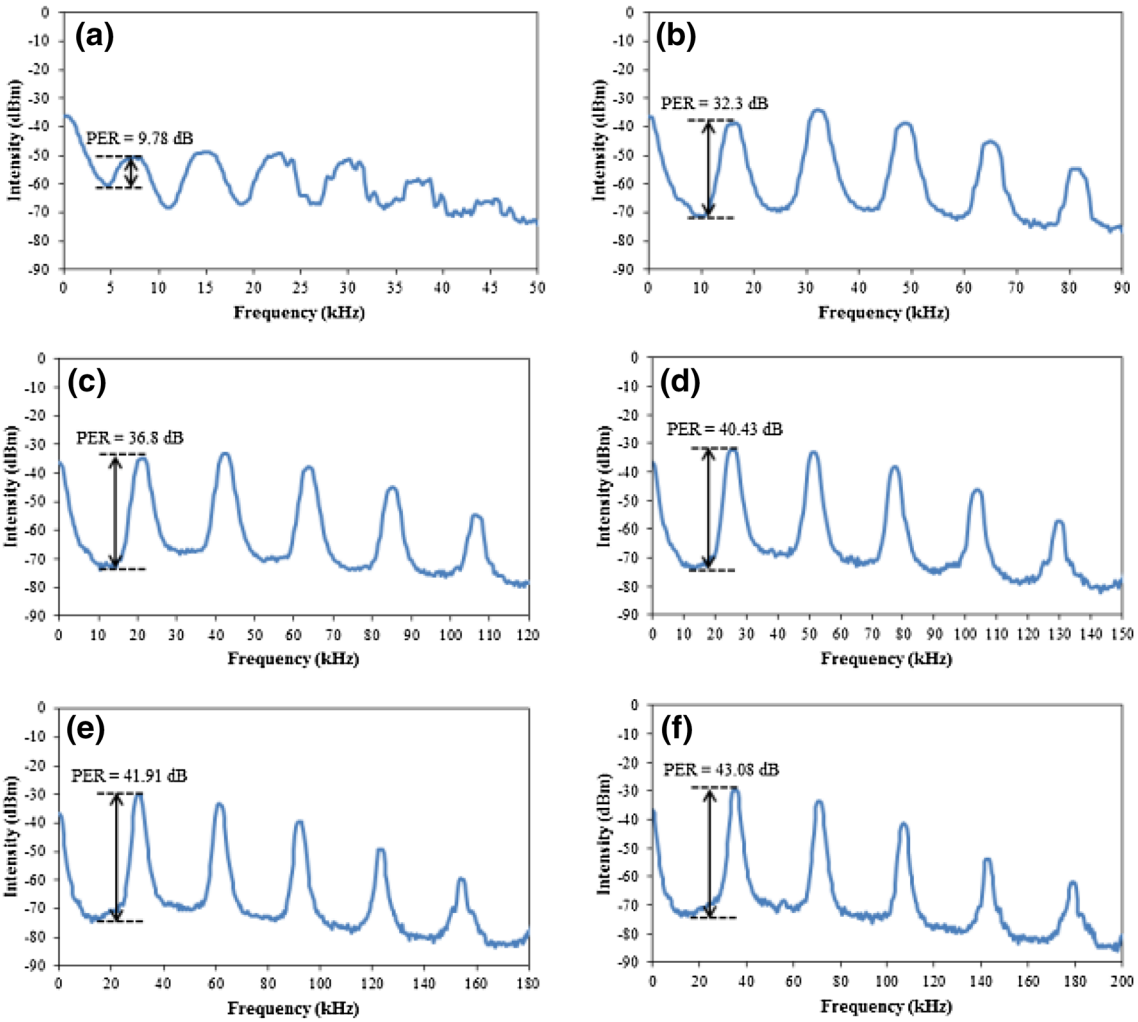

Fig. 13 RF spectrum of Q-switched EDFL incorporating WS_2-SA at the pump power of **a** 12.7 mW, **b** 35.9 mW, **c** 58.8 mW, **d** 81.6 mW, **e** 104.7 mW, and **f** 128.8 mW

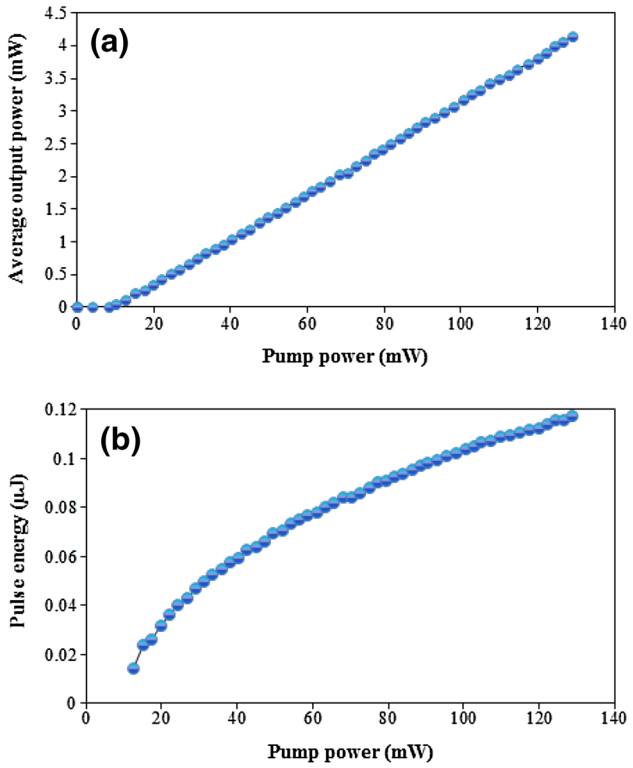

Fig. 14 **a** Average output power and **b** pulse energy of the WS2-SA-based Q-switched EDFL as a function of pump power

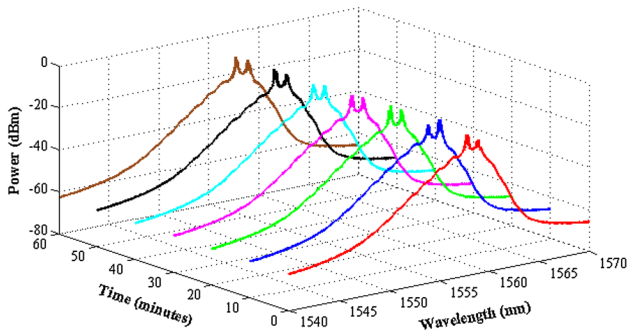

Fig. 15 Stability test of WS_2-SA-based Q-switched EDFL over an observation period of 60 min

50 dB presented in other SA-based Q-switched fiber lasers [2, 37].

The average output power and pulse energy of the WS_2-SA-based Q-switched EDFL versus the pump power are plotted in Fig. 14. The average output power develops linearly against the pump power after reaching the continuous wave lasing threshold of 10 mW as illustrated in Fig. 14a. The average output power is 4.1 mW at the maximum pump power of 128.8 mW. For every 10 mW increment in pump power, the average output power increases by approximately 0.3 mW. The pulse energy of the Q-switched EDFL is calculated by dividing the average output power to the pulse repetition rate. From Fig. 14b, the pulse energy of the WS_2-SA-based Q-switched EDFL evolves from 0.01 μJ at 12.7 mW pump power to 0.12 μJ at 128.8 mW maximum pump power. Correspondingly, the slope efficiency for the pulse energy is measured to be 0.89 μJ/W.

The stability test of WS_2-SA-based Q-switched EDFL over an observation period of 60 min at 128.8 mW pump power is presented in Fig. 15. The measurement is recorded for every 10 min time intervals. Based on the experimental observation, the Q-switched laser performance is maintained along the observation period, which validates the stability of our proposed WS_2-SA.

Table 1 summarizes the performance of Q-switched EDFL utilizing WS_2-SA. All the cited works operate within a 1560 nm wavelength range. The main criterion for the comparison is the fabrication of WS_2-SA which involves chemicals such as polymer host and solvent. It is noted that the 12.7 mW pump power threshold for initiating Q-switched operation in our work is the lowest among the listed comparisons. The pulse energy of 120 nJ generated from the proposed WS_2-SA is better than that in other published works except Ref. [41]. The proposed method of WS_2 mechanical deposition on fiber ferrule is not only simple, but also induces low loss. Therefore, the operation of Q-switching can be effectively initiated at lower pump power.

5 Conclusion

In conclusion, a Q-switched EDFL utilizing mechanically deposited WS_2-SA is proposed and demonstrated. The technique utilizes mechanical deposition of WS_2 nano-powder directly on the fiber ferrule with subsequent exfoliations to reduce the thickness of material. The fabricated WS_2-SA is characterized to have 548.6 MW/cm^2 saturation intensity, 4.1% modulation depth, and 67.8% non-saturable loss. We obtained a Q-switched laser with self-pulsing operation at 12.7 mW pump power. At the maximum pump power of 128.8 mW, the Q-switched EDFL generates output with spectral bandwidth of 2.6 nm, repetition rate of 35.2 kHz, pulse width of 2.6 μs, PER of 43.1 dB, average output power of 4.1 mW, and pulse energy of 0.12 μJ. To the best of our knowledge, this is the first application of direct mechanical deposition technique of WS_2 nano-powder onto

Table 1 Summary of Q-switched EDFL incorporating WS_2-SA with lasing wavelength around 1560 nm

Ploymer host and solvent	Coupling method	Q-switching pump power threshold (mW)	Repetition rate (kHz)	Pulse energy (nJ)	Output power (mW)	Pulse width (μs)	PER (dB)	References
Sodium cholate aqueous solution	Sandwich	252	125	46.3	5.79	//	//	[24]
Ethanol	Evanescent field	186	134	19	2.5	0.71	//	[25]
Sodium cholate and PVA solution	Sandwich	400	77.925	82.29	6.412	6.707	54.2	[29]
Ethanol	Evanescent field	295	108	72.59	7.84	1.3	//	[38]
Ethanol and PVA	Sandwich	400	51.749	59.6	3.08	4.416	58	[39]
Water or ethanol	Sandwich	40	49.2	5.89	0.29	20.33	42.7	[40]
Aqueous PVA solution	Sandwich	174	97.1	179.6	17.44	10.3	43	[41]
Fluorine mica	Sandwich	40	33.74	61.4	2.07	6.98	64	[42]
//	Sandwich	12.7	35.24	120	4.1	2.6	43.08	This work

the fiber tip for generating Q-switched pulses in fiber-based laser system. Deposition of WS_2 nano-powder through this method is simpler compared to previous methods. This work also highlights the nonlinear light absorption ability of WS_2 for potential applications in photonics and nonlinear optics.

Acknowledgements This work was supported in part by the Universiti Putra Malaysia and Ministry of Higher Education, Malaysia, under the research Grant LRGS(2015)/NGOD/UM/KPT and GP-IPB/2014/9440700.

References

1. Z. Sun, T. Hasan, F. Torrisi, D. Popa, G. Privitera, F. Wang, F. Bonaccorso, D.M. Basko, A.C. Ferrari, ACS Nano **4**, 803 (2010)
2. L.Q. Zhang, Z. Zhuo, J.X. Wang, Y.Z. Wang, Laser Phys. **22**, 433 (2012)
3. J. Xu, J. Liu, S. Wu, Q.H. Yang, P. Wang, Opt. Express **20**, 15474 (2012)
4. J. Wang, Z. Luo, M. Zhou, C. Ye, H. Fu, Z. Cai, H. Cheng, H. Xu, W. Qi, IEEE Photon. J. **4**, 1295 (2012)
5. F.B.A. Frünge, *Optical Pulses–Lasers–Measuring Techniques in Optical Pulses, Lasers, Measuring Techniques* (Academic Press, New York and London, 1965)
6. K. Yin, B. Zhang, L. Li, T. Jiang, X. Zhou, J. Hou, Photon Res. **3**, 72 (2015)
7. Z. Sun, D. Popa, T. Hasan, F. Torrisi, F. Wang, E.J.R. Kelleher, J.C. Travers, V. Nicolosi, A.C. Ferrari, Nano Res. **3**, 653 (2010)
8. A. Martinez, Z. Sun, Nat. Photon. **7**, 842 (2013)
9. P.A. Loiko, J.M. Serres, X. Mateos, J. Liu, H. Zhang, A.S. Yasukevich, K.V. Yumashev, V. Petrov, U. Griebner, M. Aguiló, F. Díaz, Appl. Phys. B **122**, 1 (2016)
10. D. Hsieh, D. Qian, L. Wray, Y. Xia, Y.S. Hor, R.J. Cava, M.Z. Hasan, Nature **452**, 970 (2008)
11. H. Zhang, C.X. Liu, X.L. Qi, X. Dai, Z. Fang, S.C. Zhang, Nat. Phys. **5**, 438 (2009)
12. J.E. Moore, Nature **464**, 194 (2010)
13. H.S.S.R. Matte, A. Gomathi, A.K. Manna, D.J. Late, R. Datta, S.K. Pati, C.N.R. Rao, Angew. Chem. Int. Ed. **49**, 4059 (2010)
14. M. Zhang, G. Hu, G. Hu, R.C.T. Howe, L. Chen, Z. Zheng, T. Hassan, Sci. Rep. **5**, 17482 (2015)
15. Q.H. Wang, K. Kalantar-Zadeh, A. Kis, J.N. Coleman, M.S. Strano, Nat. Nanotech. **7**, 699 (2012)
16. F. Bonaccorso, Z. Sun, T. Hasan, A.C. Ferrari, Nat. Photon. **4**, 611 (2010)
17. D. Hanlon, C. Backes, E. Doherty, C.S. Cucinotta, N.C. Berner, K. Lee, P. Lynch, Z. Gholamvand, A. Harvey, S. Zhang, K. Wang, G. Moynihan, A. Pokle, Q.M. Ramasse, N. McEvoy, W.J. Blau, J. Wang, S. Sanvito, D.D. Oregan, G.S. Duesberg, V. Nicolosi, J.N. Coleman, Nat. Commun. **6**, 8563 (2015)
18. R. Nie, J. She, D. Li, F. Li, B. Peng, Appl. Phys. B **122**, 241 (2016)
19. Y. Tanaka, Z. Ren, T. Sato, K. Nakayama, S. Souma, T. Takahashi, K. Segawa, Y. Ando, Nat. Phys. **8**, 800 (2012)
20. N. Kim, P. Lee, Y. Kim, J.S. Kim, Y. Kim, D.Y. Noh, S.U. Yu, J. Chung, K.S. Kim, ACS Nano **8**, 1154 (2014)
21. Y. Chen, G. Jiang, S. Chen, Z. Guo, X. Yu, C. Zhao, H. Zhang, Q. Bao, S. Wen, D. Tang, D. Fan, Opt. Express **23**, 12823 (2015)
22. P. Li, B. Liang, M. Su, Y. Zhang, Y. Zhao, M. Zhang, C. Ma, N. Su, Appl. Phys. B **122**, 1 (2016)
23. D. Mao, Y. Wang, C. Ma, L. Han, B. Jiang, X. Gan, S. Hua, W. Zhang, T. Mei, J. Zhao, Sci. Rep. **5**, 7965 (2015)
24. K. Wu, X. Zhang, J. Wang, X. Li, J. Chen, Opt. Express **23**, 11453 (2015)
25. S.H. Kassani, R. Khazaeinezhad, H. Jeong, T. Nazari, D.I. Yeom, K. Oh, Opt. Mat. Express **5**, 373 (2015)
26. R. Khazaeinezhad, S.H. Kassani, H. Jeong, D.I. Yeom, K. Oh, J. Lightwave Technol. **33**, 3550 (2015)
27. P. Yan, A. Liu, Y. Chen, H. Chen, S. Ruan, C. Guo, S. Chen, I.L. Li, H. Yang, J. Hu, G. Cao, Opt. Mat. Express **5**, 479 (2015)
28. P. Yan, A. Liu, Y. Chen, J.Z. Wang, S. Ruan, H. Chen, J. Ding, Sci. Rep. **5**, 12587 (2015)
29. B. Chen, X. Zhang, K. Wu, H. Wang, J. Wang, J. Chen, Opt. Express **23**, 26723 (2015)
30. A. Martinez, K. Fuse, S. Yamashita, Appl. Phys. Lett. **99**, 121107 (2011)
31. A. Berkdemir, H.R. Gutiérrez, A.R. Botello-Méndez, N. Perea-López, A.L. Elías, C.I. Chia, B. Wang, V.H. Crespi, F.

López-Urías, J.C. Charlier, H. Terrones, M. Terrones, Sci. Rep. **3**, 1755 (2013)
32. H. Zeng, G.-B. Liu, J. Dai, Y. Yan, B. Zhu, R. He, L. Xie, S. Xu, X. Chen, W. Yao, X. Cui, Sci. Rep. **3**, 1608 (2013)
33. R. Khazaeinezhad, S.H. Kassani, T. Nazari, H. Jeong, J. Kim, K. Choi, J. Lee, J.H. Kim, H. Cheong, D. Yeom, K. Oh, Opt. Commun. **335**, 224 (2015)
34. H. Ahmad, K.Z. Hamdan, F.D. Muhammad, S.W. Harun, M.Z. Zulkifli, Appl. Phys. B **118**, 269 (2015)
35. P.A. Bertrand, Phys. Rev. B **44**, 5745 (1991)
36. R. Herda, S. Kivisto, O.G. Okhotnikov, Opt. Lett. **33**, 1011 (2008)
37. Z. Yu, Y. Song, J. Tian, Z. Dou, H. Guoyu, K. Li, H. Li, X. Zhang, Opt. Express **22**, 11508 (2014)
38. R. Khazaeinezhad, T. Nazari, H. Jeong, K.J. Park, B.Y. Kim, D.-I. Yeom, K. Oh, IEEE. Photon. J. **7**, 1503507 (2015)
39. B. Chen, H. Wang, X. Zhang, J. Wang, K. Wu, J. Chen, OECC **2015**, 1 (2015)
40. H. Ahmad, N.E. Ruslan, M.A. Ismail, S.A. Reduan, C.S.J. Lee, S. Sathiyan, S. Sivabalan, S.W. Harun, Appl. Opt. **55**, 1001 (2016)
41. G. Hu, M. Zhang, L. Chen, X. Zhu, G. Hu, R. C. T. Howe, X. Zhao, Z. Zheng, T. Hasan: Fio/LS OSA 2015, FM3G-5 (2015)
42. L. Li, Z. Wang, Y. Wang, X. Wang, G. Yang, S. Jiang, Laser Phys. **26**, 105105 (2016)